Effect of pore size on tissue ingrowth and osteoconductivity in biodegradable Mg alloy scaffolds

Julia Augustin[1] iD **, Franziska Feichtner[1], Anja-Christina Waselau[1], Stefan Julmi[2], Christian Klose[2], Peter Wriggers[3], Hans Jürgen Maier[2] and Andrea Meyer-Lindenberg[1]**

Abstract

Magnesium has mechanical properties similar to those of bone and is being considered as a potential bone substitute. In the present study, two different pore sized scaffolds of the Mg alloy LAE442, coated with magnesium fluoride, were compared. The scaffolds had interconnecting pores of either 400 (p400) or 500 µm (p500). ß-TCP served as control. Ten scaffolds per time group (6, 12, 24, 36 weeks) were implanted in the trochanter major of rabbits. Histological analyses, µCT scans, and SEM/EDX were performed. The scaffolds showed slow volume decreases (week 36 p400: 9.9%; p500: 7.5%), which were accompanied by uncritical gas releases. In contrast, ß-TCP showed accelerated resorption (78.5%) and significantly more new bone inside ($18.19 \pm 1.47\,mm^3$). Bone fragments grew into p400 ($0.17 \pm 0.19\,mm^3$) and p500 ($0.36 \pm 0.26\,mm^3$), reaching the centrally located pores within p500 more frequently. In particular, p400 displayed a more uneven and progressively larger surface area (week 36 p400: 253.22 ± 19.44; p500: $219.19 \pm 4.76\,mm^2$). A better osseointegration of p500 was indicated by significantly more trabecular contacts and a 200 µm wide bone matrix being in the process of mineralization and in permanent contact with the scaffold. The number of macrophages and foreign body giant cells were at an acceptable level concerning resorbable biomaterials. In terms of ingrown bone and integrative properties, LAE442 scaffolds could not achieve the results of ß-TCP. In this long-term study, p500 appears to be a biocompatible and more osteoconductive pore size for the Mg alloy LAE442.

Keywords

Pore size, osseointegration, bone ingrowth, osteoconductivity, LAE442

Introduction

The use of autologous bone in larger bone defects is limited by availability, surgical effort, and additional risks at the donor site.[1] As an alternative, the development of bone substitute materials over the last two decades has been increasingly focused on alloys with a high magnesium (Mg) content.[2–16] In some cases, however, animal studies showed that the initially promising Mg alloys showed too rapid degradation behavior in vivo,[8,11,16] or they were classified as insufficiently biocompatible.[8,10,12] The Mg alloy LAE442 has shown the most promising results after intraosseous implantation in several animal models (guinea pig,[2,17] rabbit,[3,4,18,19] and sheep[20]). Corrosion retardation, stable mechanical properties, and an acceptable immune response of the host tissue to the foreign material have been observed for this alloy in recent years.[2–4,18–20]

[1]Clinic for Small Animal Surgery and Reproduction, Ludwig-Maximilians-Universität, Munich, Germany
[2]Institut für Werkstoffkunde (Materials Science), Leibniz Universität Hannover, Garbsen, Germany
[3]Institute of Continuum Mechanics, Leibniz Universität Hannover, Garbsen, Germany

Corresponding author:
Andrea Meyer-Lindenberg, Clinic for Small Animal Surgery and Reproduction, Ludwig-Maximilians-Universität, Veterinärstraße 13, Munich 80539, Germany.
Email: ameylin@lmu.de

The material structure, surface finish and surface treatments,[21,22] stability and surgical technique,[11,23,24] as well as the health status of the patients[25–27] are considered as multiple factors that can influence bone remodeling and biocompatibility of the implant.[24] Functionality also depends on early revascularisation of the defect to provide osteogenic precursor cells, nutrients, and locally acting growth factors for further differentiation of new bone.[28,29] Slowly biodegradable Mg alloys have the great advantage of providing long-term stability within the defect site, while allowing ingrowth of new bone at the same time as degradation occurs.[22,29] This desired effect was described by Phemister[30] at the beginning of the last century as "creeping substitution." Porous scaffolds made of ceramics, composites, and titanium encourage the ingrowth of granulation tissue as well as bone tissue,[28,31–36] and thus promote the osteoconductive properties of the bone substitute material.[29] Initial studies on porous implants have shown that pore sizes of 100 μm are the minimum size required for the transport of cells and nutrients into the interior of porous scaffolds.[37] Pore sizes above 300 μm are considered to be particularly beneficial for blood vessel supply and osteogenesis.[28,29,33] Porous Mg implants have also been used in vivo. Osteogenesis is observed in Mg implants with pore sizes between 100 μm and over 400 μm, which are used as pure Mg or as main element of an alloy.[6,7,14,15] Studies by Lalk et al.[7] and Cheng et al.[14] showed that Mg scaffolds are well suited as a matrix for bone-scaffold contacts and cell adaptation, and therefore anchoring of the bone substitute material into the adjacent bone. The interaction between scaffold and bone is a requirement for the successful osseointegration of the Mg scaffold during its degradation in the bone tissue.[24,38] So far only solid LAE442 implants have been investigated[2–4,11,18–20,39] and have achieved promising results with regard to peri-implant bone formation.[2,3,5,11,18–20] LAE442 was used the first time in the form of open-pored scaffolds, with two firmly defined and always homogeneously reproducible pore size models in the study by Augustin et al.[40] Associated investigations on the clinical tolerability as well as μCT measurements of the outer scaffold and bone environment provided promising results. Using high-resolution ex vivo μCT80 scan images, SEM/EDX images, and histological tissue samples, the objective of the present study was to investigate which pore size model is more suitable as an osteoconductive and therefore potentially more suitable bone substitute for osteoneogenesis. Degradation behavior, interaction with surrounding bone structure and cellular tissue reactions over a period of up to 36 weeks were investigated and compared between both LAE442 pore size models.

Materials and methods

Production and characteristics of the scaffolds

The Mg alloy LAE442 (90 wt.% Mg, 4 wt.% Li, 4 wt.% Al, 2 wt.% rare earth) was prepared using the alloy LAE442 according to the method proposed by Seitz et al.[41] In advance of the actual manufacturing process of the investment casting, the casting molds for the scaffolds were made with a 3D printer (Solidscape, Inc., Merrimack, USA) in individual superimposed wax layers.[42]

Two versions of the LAE442 scaffolds (Ø 4 mm, height 5 mm) were produced (*n* = 40 each). These had homogeneously distributed, interconnecting pores, marked out by intermediate struts. The first model (p400) had an average pore size of 400 μm, a strut thickness of 0.3–0.4 mm and a porosity of 43.4%. The second model (p500) had an average pore size of 500 μm a strut thickness of 0.4–0.5 mm and a porosity of 41.4% (Figure 1(a) and (b)). The LAE442 scaffolds were additionally coated with magnesium fluoride (MgF_2).[39,43] The control group implants were commercially available resorbable beta-tricalcium phosphate (ß-TCP) implants (Cerasorb M, Curasan AG, Kleinostheim, Germany), with the same dimensions (Ø 4 mm, height 5 mm) with a porosity of 65% (pore sizes ≤500 μm) (Figure 1(c)). All Mg scaffolds were sterilized by gamma irradiation of >29 Gry (BBF-Sterilisationsservice GmbH, Kernen, Germany).

Animal model

The animal experiments were approved by the regional government of Upper Bavaria in accordance with § 8 of the Animal Welfare Act (reference number ROB 55.2-1-54-2532-181-2015). Sixty adult, female Zika rabbits (Assamhof, Kissing, Germany) with an average weight of 3.9 kg (±0.3 kg) were randomly divided into scaffold and time groups (6, 12, 24, or 36 weeks). According to Lalk et al.,[6] two scaffolds (one per left and right hind limb) were implanted in the cancelous part of the greater trochanter of the femur. For each scaffold group (p400, p500, and ß-TCP) a total of 40 scaffolds were used (*n* = 10 per time group). The animals were kept according to the European Directive on the housing of experimental animals (Appendix A, ETS 123). In addition to the rationed commercial pellet feed (Kanin Kombi, Rieder Asamhof GmbH & Co. KG, Kissing, Germany), the animals had access to hay and water ad libitum.

Operation

Anesthesia was induced by intramuscular administration of 0.15 mg/kg ketamine (Anesketin® 100 mg/ml, Albrecht GmbH, Aulendorf, Germany) and 0.25 mg/kg medetomidine (Dorbene vet® 1 mg/ml, Zoetis Deutschland GmbH, Berlin, Germany). A venous catheter was placed into the auricular vein and the animals were intubated. After routine preparation of an aseptic surgical field, anesthesia was maintained with an isoflurane/oxygen mixture (1.5–2 vol.-% with simultaneous oxygen supply of 1 l/min). In addition, the animals were given a fentanyl infusion 10 μg/kg/h μg/ml (Fentadon®, 50 μg/ml, CP-Pharma Handelsgesellschaft mbH, Burgdorf, Germany) during surgery
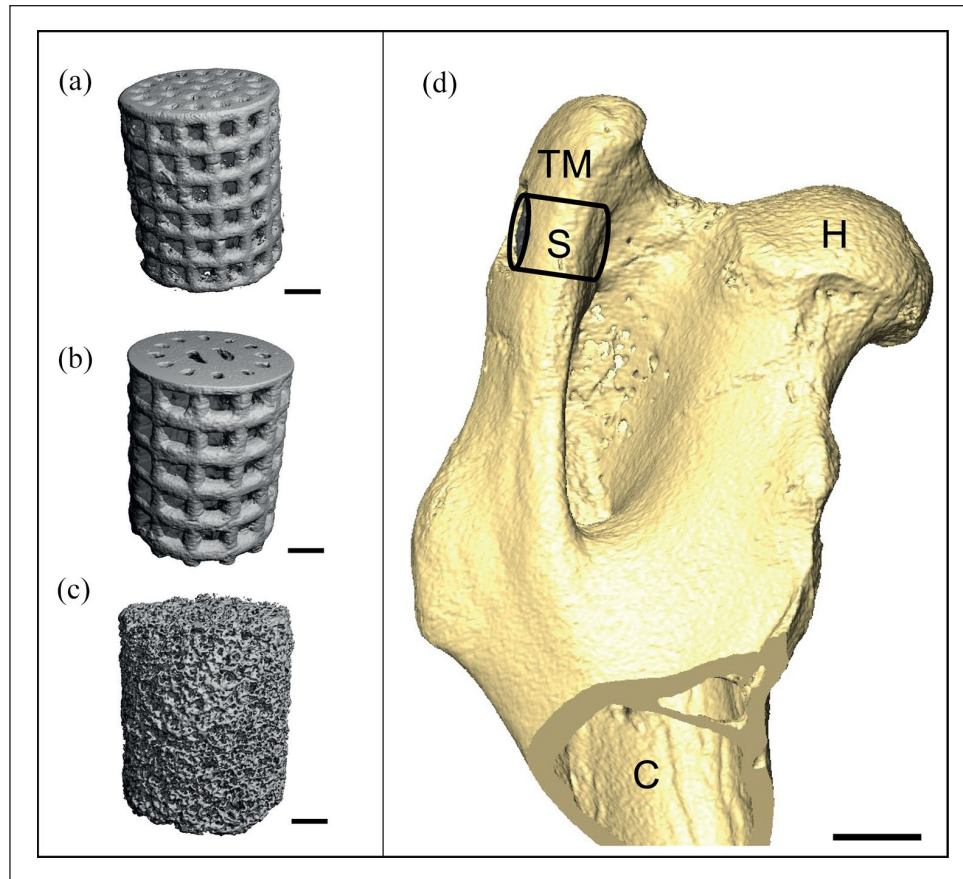
Figure 1. Models of open-pored scaffolds: (a) LAE442 p400, (b) LAE442 p500, (c) ß-TCP (control); scale bar: 1 mm, and (d) medial view of the implantation site; S: scaffold; H: femur head; C: medullary cavity; TM: Trochanter major, scale bar: 5 mm.

to ensure analgesia. Surgical access was performed as described by Lalk et al.[6] through a 2 cm long skin incision, preparation of the underlying fat tissue and the musculature up to the greater trochanter of the femur with a raspatory. A 6 mm deep hole was drilled into the greater trochanter (Colibrii II, Synthes GmbH, Oberdorf, Switzerland; drill head: Ø 4 mm) and the implant was inserted (Figure 1(d)). The wound was sutured in layers with absorbable sutures (Monosyn® 4/0, B. Braun Surgical S.A., Rubi, Spain) and the skin was closed by single stitches (Optilene® 4/0, B. Braun Surgical S.A., Rubi, Spain). The animals received a single intravenous administration of 20 µg/kg buprenorphine (Bupresol®, 0.3 mg/ml, CP-Pharma Handelsgesellschaft mbH, Burgdorf, Germany) for postoperative analgesia. From the time of surgery up to the fifth post-operative day, oral administration of 10 mg/kg/day enrofloxacin (Enrobactin®, 25 mg/ml, CP-Pharma Handelsgesellschaft mbH, Burgdorf, Germany) and 0.3 mg/kg/day meloxicam (Rheumocam®, 1.5 mg/ml, Boehringer Ingelheim Pharma GmbH & Co. KG, Ingelheim am Rhein, Germany) was given. The general condition of the animals, as well as wounds and lameness, were monitored daily.

Euthanasia

At the end of the respective observation periods, the animals were euthanized with 5 mg/kg propofol (Narcofol®, 10 mg/ml, CP-Pharma Handelsgesellschaft mbH, Burgdorf, Germany) and 1 ml/kg pentobarbital (Narkodorm®, 182.3 mg/ml, CP-Pharma Handelsgesellschaft mbH, Burgdorf, Germany). Equally sized blocks (1.5 cm × 1.5 cm) of the bone containing the scaffold were cut with a diamond band saw (Walter Messner GmbH, Osteinbek, Germany). These were fixed with 4% formalin solution (Carl Roth GmbH u. Co.KG, Karlsruhe, Germany) for further ex vivo examinations.

Ex vivo µCT80

With the exception of ß-TCP, scans of the LAE442 scaffolds were taken prior to implantation and scans of all scaffold groups were taken after the in vivo observation period (6, 12, 24, 36). Each bone-scaffold compound was scanned using µCT80 tomography (Scanco Medical AG, Brüttisellen, Switzerland), with a resolution of 10 µm, a tube current of 114 µA, a tube voltage of 70 kVp and an integration time of 600 ms. The tomograms showed the

Table 1. Scoring system employed for µCT80. Parameters were evaluated over the entire cross-sectional area of each scaffold per investigation time. Score 0 stands for the desired score, or rather the score where no change has been detected.

Scoring Parameter	Score 0	1	2	3	4
Scaffold degradation*	None	Small degradation layer	Clearly visible degradation layer	>50% Degradation area scaffold	Completely degraded
Scaffold shape*	Original	Mild changes in surface topography	Moderate altered shape	>50% Clearly altered surface	Loss of shape
Gas -Within scaffold -Adjacent	None	Sporadically/few	Moderate	Many >50% of the pore voids	Pores are totally filled with gas
Drill hole closure	Closed	Small gap	50% Closed	Large gap	Open
Osseointegration (bone-scaffold contacts)	Large amounts of bone-scaffold contacts, no/few gaps	Moderate contacts with several trabeculae	Few trabecular contacts, several gaps between	One direct contact	None

*Parameters were only evaluated for LAE442 p400 and p500.

scaffolds in longitudinal axis. Using the µCT evaluation program (V 6.4-2, Scanco Medical AG, Zurich, Switzerland), the scaffolds were reoriented into standardized cross-sectional views and further analyzed.

Evaluation of structural scaffold characteristics and scaffold integration

The structural parameters degradation, shape, and gas formation (in the scaffold/in the immediate vicinity) were investigated with a semi-quantitative 2D analysis of the cross sections. A modified scoring system based on Lalk et al.[6] was used for each scan. The scores ranged from 0 for "unchanged or physiological" up to 4 for "significantly changed characteristics." In addition, remaining drill hole diameters were measured (cf. Table 1). For ß-TCP, the semi-quantitative parameters degradation and scaffold shape were evaluated descriptively, due to a more irregular pore distribution compared to LAE442 p400 and p500 and different material origin. The parameters drill hole and gas in ß-TCP could be evaluated analogous to LAE442.

The osseointegration of LAE442 p400, p500, and ß-TCP was evaluated by the existence of bone-scaffold contacts (Figure 2) and new bone in the scaffold (central part – CP/ outer part – OP) (Figure 2(a) and (b)). For the scaffold structure evaluation, six successive cross-sectional layers (Figures 2 and 3(a): LAE442, alternating strut-/pore-layers; ß-TCP layers in corresponding distances) were considered and evaluated semi-quantitatively according to Table 1. In addition, the bone structure in the vicinity of all scaffold groups was examined descriptively.

Degradation and bone ingrowth

Quantitative 3D measurements were performed using two cylindrical shapes in combination with the specific thresholds of the scaffolds (ß-TCP: 360, LAE442: 160, bone: 186), as described by Lalk et al.[7] The first shape ("Bone-in")

corresponded exactly to the outer cross-sectional contour of the scaffolds and included the bone which has grown into the scaffold pores (Figure 2(c) and (d)). Starting from the cylindrical shape "Bone-in," a second shape ("Bone-ex") was created, which always excluded the bone and thus only represented the LAE442 scaffold material (Figure 2(e) and (f)). For the quantitative 3D evaluation of the LAE442 scaffolds volume (mm^3) and surface area (mm^2) were determined for the respective time periods based on the "Bone-ex" cylinder. The parameter ingrown bone (mm^3) within the p400 and p500 pores of LAE442 represented the difference between the values determined for both cylindrical shapes (Ingrown bone = "Bone-in"– "Bone-ex"). For ß-TCP, the values volume and surface area were determined using the specific threshold. The ingrown bone within ß-TCP could be calculated by the bone threshold value, which clearly differed from ß-TCP.

Electron microscopy

One histological cross-section per pore size and time group of the LAE442 scaffolds was selected for analysis in the scanning electron microscope (SEM) to determine possible changes in the base material (non-corroded Mg alloy) and the degradation layer on the scaffold struts over time. Energy dispersive X-ray spectroscopy (EDX) was used to investigate elemental distributions of the base material, degradation layer, and precipitates on the degradation layer. The composition of bone and osteoid-like tissue (OLT) was determined inside and outside the porous LAE442 scaffolds for comparison. Since the EDX analyses required unstained samples, it was very difficult to reliably measure OLT that might be present within a sample without first being able to distinguish it by color or by a sufficient degree of mineralization and thus localize it. The measurement was successfully carried out once on a p500 sample, as here the seam of the OLT was thick enough to reliably identify the corresponding area. The analyses
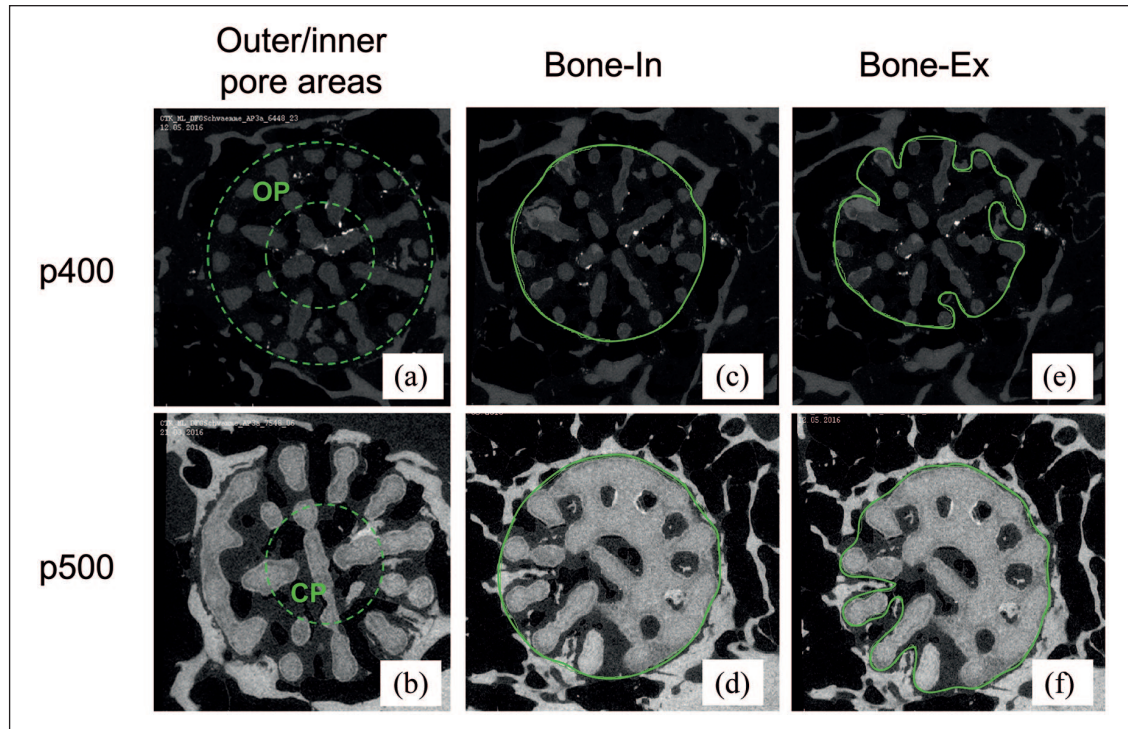
Figure 2. Outer pore area (= OP) and central/inner pore area (= CP) of the scaffolds (a and b); contours (c and d) representing "Bone-in" and (e and f) "Bone-Ex."
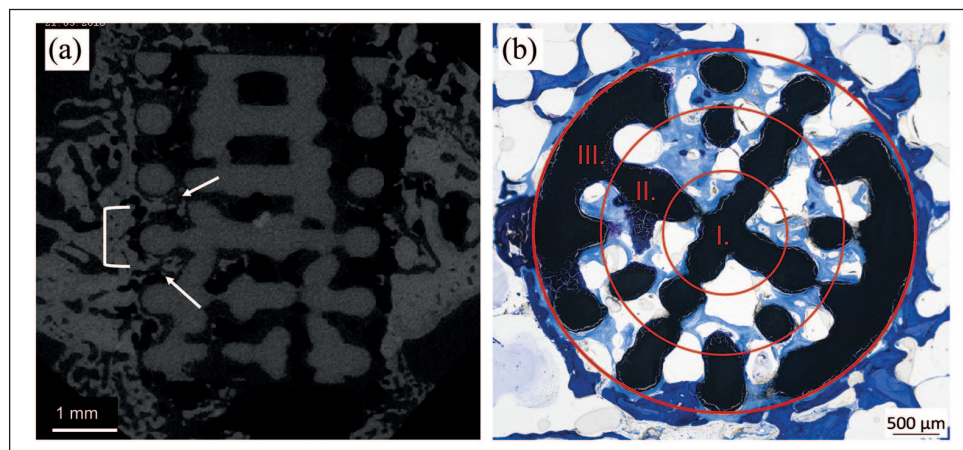
Figure 3. (a) Longitudinal view of a LAE442 scaffold with pores and struts; white arrows: ingrowth of new bone; white bracket: pore-layers with an intermediate strut layer and (b) histological cross-section, regions I.–III. (scaffold center, middle part, and outer part).

were performed with the SUPRA 55 VP (Carl Zeiss AG, Oberkochen, Germany), a voltage of 15 kV and a working distance of 20–25 mm (overview) respectively 7.8–9.8 mm (close-up).

Histological examinations

The scaffold containing bone samples were fixed in 4% formalin and dehydrated in an ascending alcohol series. After incubation with xylene, the samples were embedded in Technovit® 9100 (Heraeus Kulzer GmbH, Wehrheim, Germany), according to the manufacturer's instructions. The polymerized blocks were mounted on plastic slides with precision adhesive (Technovit® 7210 VLC, Heraeus Kulzer GmbH, Wehrheim, Germany). Histological thick sections (40 μm) of the scaffold samples were prepared by the cutting and grinding technique according to Donath and Breuner[44] with a diamond band saw and grinding machine (cut grinder and lap grinder, Walter Messner, Oststeinbek, Germany). The central cross-sections were

Table 2. Scoring system employed for semiquantitative histological evaluation. Parameters were evaluated using one cross-section per scaffold (* was only rated for LAE442 p400 and p500).

Scoring parameter	Score 0	1	2	3
Material changes (Granulation/Cracks)*	None	Locally	Many	Severe
	0%	1%–25%	26%–50%	>50%
New Bone (NB)	None	Sporadically/few	Moderate	Many
	0%	1%–10%	11%–25%	>25%
Osteoid-like tissue (OLT)*	None	Sporadically/few	Moderate	Many
	0%	1%–10%	11%–25%	>25%
Fibrous tissue	None	Sporadically/few	Moderate	Many
	0%	1%–10%	11%–25%	>25%
Vascularization	None	Sporadically/few	Moderate	Many
Foreign body reaction (Macrophages/Foreign body giant cells)	None	Sporadically/few	Moderate	Many
Inflammation (Lymphocytes and Granulocytes)	None	Sporadically/few	Moderate	Many
Formation of a fibrous capsule	No	Yes		

stained with toluidine blue (0.1% toluidine blue O, Waldeck, Münster, Germany).

The cross sections were used for a standardized, semi-quantitative analysis in three areas (Figure 3(b)): scaffold center (I), middle part (II), and outer part of the scaffold (III). In these areas scaffold material, new bone tissue (NB) as well as osteoid-like tissue (OLT), fibrous tissue, vascularization, and possible capsule formation were examined according to Table 2. Furthermore, cellular reactions due to the occurrence of inflammatory cells were evaluated. Macrophages and foreign body giant cells (FBGC) were evaluated at 200-/100-fold magnification (Axio Imager Z.2, Carl Zeiss Microscopy GmbH, Jena, Germany).

Statistics

The statistical analysis was performed using Microsoft Office Excel® Version 2016 (Microsoft Office Professional Plus 2016, Microsoft Corporation, Redmond, USA) and SPSS® Version 25.0 (SPSS, IBM Company, Chicago, USA). The data were displayed as mean values ± standard deviations within each scaffold and time group. The independent, non-normally distributed data were tested for statistical significance using the Kruskal-Wallis test followed by Bonferroni post hoc correction. For parameters that could only be compared between the two pore sizes of LAE442, due to the different degradation behavior of Mg compared to the ß-TCP ceramic, the Mann-Whitney U-test was applied (Table 1: scaffold degradation, shape). Statistically significant differences were defined as $p < 0.05$.

Results

### Analyses in the ex vivo μCT80

Evaluation of structural scaffold characteristics. At week 6, degradation was visible in the cross-sectional views of the LAE442 scaffolds with a darker seam at the outer edge of the scaffolds compared to the μCT80 scans taken before implantation. This seam increased over time toward the inside of the scaffold and was partially visible from week 12 onward at the inner strut elements of the scaffolds of both pore sizes (Figure 4(a)).

After assessing the scaffold shape, it was noticeable for p400 that in week 6 isolated pitting corrosion occurred on the struts, which increased in the further time groups week 24 (5/10) and 36 (3/10). In addition, individual pieces of material in the upper and lower scaffold third were detached in week 36 (4/10), which lead to a partial loss in implant shape. In comparison, p500 maintained its overall cylindrical shape up to week 36, despite minor surface irregularities (8/10) and cracks (2/10) (Figure 4(b)). However, the ß-TCP scaffolds completely lost their cylindrical shape from week 12 to week 24. At week 24 and 36, only a few ß-TCP particles were visible as small bright white spots within bone trabeculae.

For both LAE442 pore sizes, gas could be detected inside and outside the scaffold at all times. The amount of gas inside p500 decreased continuously over the course of the study period until only tiny bubbles were found between the scaffold structure at week 24 and 36. The amount of gas in p400 was significantly increased compared to p500, especially in week 24 ($p = 0.023$) and did not decrease until week 36. In the scaffold surroundings, gas was distributed between the trabecular meshwork of the bone without significant difference between the pore size groups. As expected, gas formation never occurred with ß-TCP (Figure 4(c) and (d)).

The drill holes were closed in 8/10 cases in the 6-week group of p500, and in 9/10 cases in ß-TCP. In the group with the smaller pore size p400, 6/10 drill holes were completely closed in the 6- and 12-week group and 7/10 after 36 weeks. Apart from individual cases in week 6 (1/10), week 12 (3/10), and week 24 (1/10), the majority of drill holes were completely closed at all times in the ß-TCP group (Figure 4(e)).
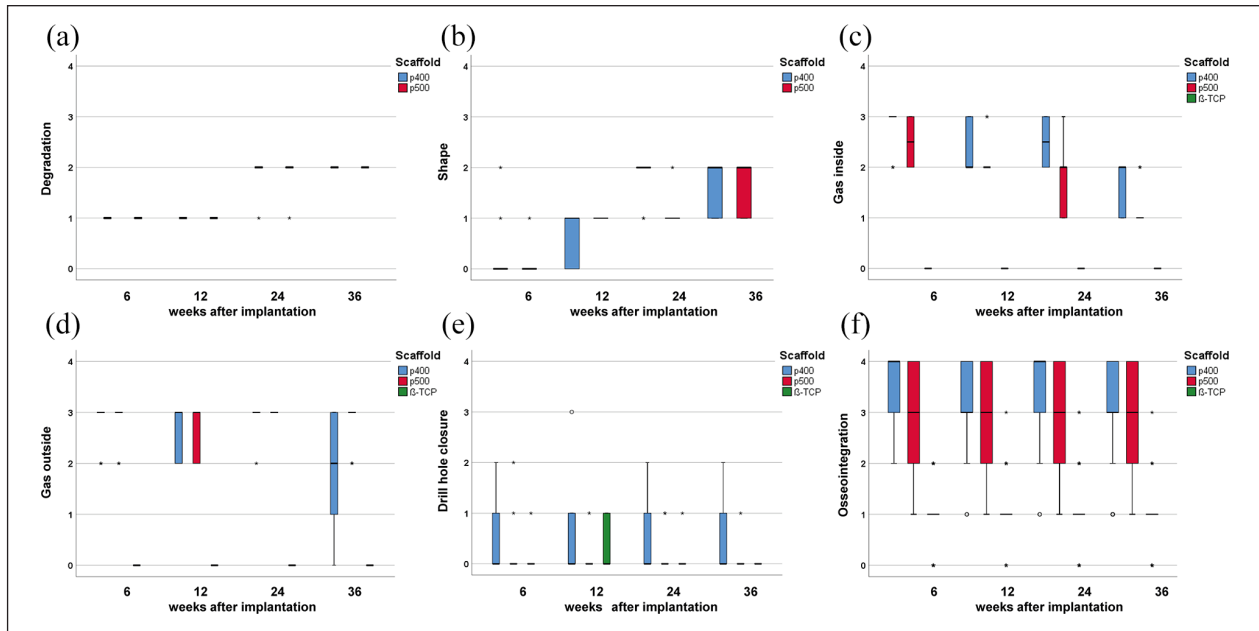
Figure 4. Box plots of: (a) scaffold degradation, (b) scaffold shape, (c) gas inside, (d) gas outside, (e) drill hole closure, and (f) scaffold osseointegration (µCT80 scans). Score 0: unchanged/good osseointegration behavior, score 4: significant changes/poor osseointegration behavior.

Evaluation of the scaffold integration. Although bone was already present in the adjacent area of LAE442 p400 at week 6, only single, thin trabeculae ($<150\,\mu m$) approached the scaffolds directly. In comparison, LAE442 p500 always had significantly more bone contact sites from week 6 onward ($p \leqslant 0.003$). From week 12, both LAE442 pore sizes showed partially ingrown trabeculae, which were often arranged in a semi-circle around the scaffold cross sections at a small distance and sporadically touched the implant surface (Figure 2). However, for ß-TCP significantly more trabeculae were in contact with the scaffold surface ($p < 0.001$). The trabeculae grew gradually in ß-TCP and became thicker or crosslinked over time (Figure 4(f)).

When evaluating the distribution pattern of new bone within the LAE442 scaffolds, all sectional scan images showed that there was always more bone in the outer pore area than in the inner area, regardless of a denser strut layer or a more open pored layer (Figure 2). Overall, p500 had more bone in both areas than p400 ($p \leqslant 0.008$). Macroscopically, the surrounding bone structure differed significantly between ß-TCP and the two LAE442 scaffolds. Overall, widely meshed cancelous bone was found around ß-TCP after 6 weeks. In the vicinity of LAE442 p400 and p500, a dense trabecular meshwork with thicker and thinner trabeculae was found from week 6 onward, which was interspersed with gaps.

Analysis of scaffold degradation and bone ingrowth. The 3D evaluation of the data sets regarding density and volume of p400 and p500 showed uniform degradation behavior of the porous Mg alloy during their respective observation periods. Compared to the values before implantation, a slowly progressive volume loss continued in both LAE442 pore sizes (residual volume week 36: p400: $90.1 \pm SD$ 3.1% and p500: $92.5 \pm SD$ 2.0%). The residual volume of ß-TCP was $21.5 \pm SD$ 1.4% in week 36 compared to the chosen reference value in week 6. In both LAE442 pore sizes, degradation was accompanied by a slight increase in surface area until week 36 (p400) and week 24 (p500), respectively. ß-TCP decreased its surface area significantly over the determined time period. Higher amounts of newly ingrown bone could be detected for p500 in direct comparison between both LAE442 pore sizes but did not lead to significant differences. The markedly higher bone values of ß-TCP, which did not change after week 12, were significantly different from those of p400 and p500 at all times ($p < 0.001$) (Table 3).

SEM/EDX: Surface characteristics and element distribution. The LAE442 cross-sections selected for the SEM images showed a narrow and dark degradation layer on the outer scaffold edges for both pore sizes at week 6. Compared to the non-corroded material in more central areas, the Mg content in the degradation layer was slightly reduced based on EDX examinations (Figure 5). In contrast, the aluminum (Al) content in the degradation layer was always slightly higher than in the centrally located non-corroded material. Rare earths (SE) were always detected in both areas (degradation layer/non-corroded material) of the Mg alloy as bright evenly distributed spots (Figure 5(a), (b), and (d)). Fluorine (F) was detected once

Table 3. µCT80 measurements of scaffold volume, surface, and bone ingrowth of the different pore sizes and ß-TCP over an investigation period up to 36 weeks after implantation.

Scaffold model	Measured value (µCT80) Mean values ± SD/Max/Min	6 weeks	12 weeks	24 weeks	36 weeks
LAE442 p400	Volume (mm³)	33.32 ± 1.32/33.68/31.62	34.61 ± 1.57/37.14/31.68	32.19 ± 2.69/38.86/31.52	30.24 ± 3.09/37.61/30.95
	Surface (mm²)	245.5 ± 11.63/257.9/229.43	247.76 ± 6.52/257.11/239.2	250.47 ± 19/277.87/224.98	253.22 ± 19.44/275.84/217.11
	Bone ingrowth (mm³)	0.43 ± 0.22/0.75/0.23	0.22 ± 0.35/1.1/0.02	0.13 ± 0.11/0.31/0.00	0.17 ± 0.19/0.60/0.03
LAE442 p500	Volume (mm³)	35.19 ± 2.03/38.83/33.32	34.71 ± 2.12/37.81/33.04	34.61 ± 1.26/38.76/34.68	33.87 ± 2.00/40.17/34.76
	Surface (mm²)	182.12 ± 34.62/223.35/135.36	217.42 ± 7.59/229.87/203.58	226.22 ± 11.68/243.63/208.22	219.19 ± 4.76/228.22/211.29
	Bone ingrowth (mm³)	0.55 ± 0.45/1.34/0.02	0.18 ± 0.16/0.48/0.05	0.16 ± 0.07/0.25/0.08	0.36 ± 0.26/0.73/0.13
ß-TCP	Volume (mm³)	11.81 ± 1.95/16.29/9.94	6.82 ± 1.69/9.79/4.55	3.89 ± 1.31/6.07/1.72	2.54 ± 1.44/5.84/1.40
	Surface (mm²)	666.2 ± 66.31/810.94/603.61	396.38 ± 96.57/542.77/260.91	216.12 ± 54.63/301.98/174.83	140.72 ± 59.18/280.68/102.62
	Bone ingrowth (mm³)	24.29 ± 2.44/27.46/20.55	18.66 ± 2.44/22.28/14.48	19.09 ± 3.65/24.83/14.84	18.19 ± 1.47/20.17/15.92

at p400 in the outer edges of the degradation layer at week 6. Calcium (Ca) and phosphorus (P) were found in the degradation layer as well as in the form of white precipitates, which were directly adjacent to the degradation layer. The precipitates seemed to represent a contact between implant and mature bone at the bone-scaffold interface (Figure 5(c), (e), and (f)). The individual quantity of elements at the tested locations of the sample (according to Figure 5) are shown in Table 4. An element comparison between new bone tissue inside the LAE442 scaffolds and mature bone outside showed similar element contents of Mg, Al, Ca, P, and F. Another individual comparison in one of the p500 samples between OLT inside the scaffold and mature bone outside revealed lower Ca (1/3 of mature bone) and P (1/4 of mature bone) contents in the OLT (Figure 6). From week 12 onward, cracking occurred in the outer areas of the struts. The scaffold surface appeared more irregular in p400 than in p500 in the investigated samples.

Histology. While LAE442 scaffolds of both pore sizes macroscopically completely maintained their shape until week 36, ß-TCP showed a significant loss of shape from week 12 onward ($p \leq 0.004$). For p400 and p500, granulation of the scaffold edges occurred already from week 6 onward (Figure 7(a)–(h)). The scaffold granulation was visible by a change in the color of the initially deep black Mg alloy to increasingly gray-blue granulated areas in the degradation layer. Although p400 showed increased cracking on the scaffold struts until week 24 (Figure 8), this difference was only significant in week 12 compared to p500 ($p = 0.035$). New bone (NB) of dark blue color was visible in individual areas in week 6 in both LAE442 pore sizes. However, no significant differences between the pore size groups were observed. ß-TCP showed significantly more NB from week 12 onward compared to the two LAE442 pore sizes ($p \leq 0.002$). The trabecular structure of the NB of ß-TCP was cross-linked, while NB in p400 and p500 consisted of rather individually distributed regions within the implants (Figure 7(c)–(f)). It was apparent for both LAE442 pore sizes, that NB mostly had no direct contact with the Mg alloy inside the pores and was located in the middle of a light blue osteoid-like tissue (OLT). This tissue appeared to be less mineralized than mature bone due to its light blue coloration (Figures 7(a)–(h) and 8(a), (c), and (d)). The OLT inside the scaffold became increasingly present from week 12 onward and showed rows of overlying osteoblasts (Figure 8(a)) and osteocytes distributed in its matrix (Figure 8(a), (c), and (d)). From week 12 onward, p500 tended to have more OLT within its pores than p400, which was significant at week 24 ($p = 0.019$). OLT increased in both pore sizes over time. In ß-TCP, OLT was not observed at any time and only NB and osteoid were detected (Figure 7(a) and (b)).

Granulation tissue containing blood vessels and gas vacuoles were visible in the pores of p400 and p500
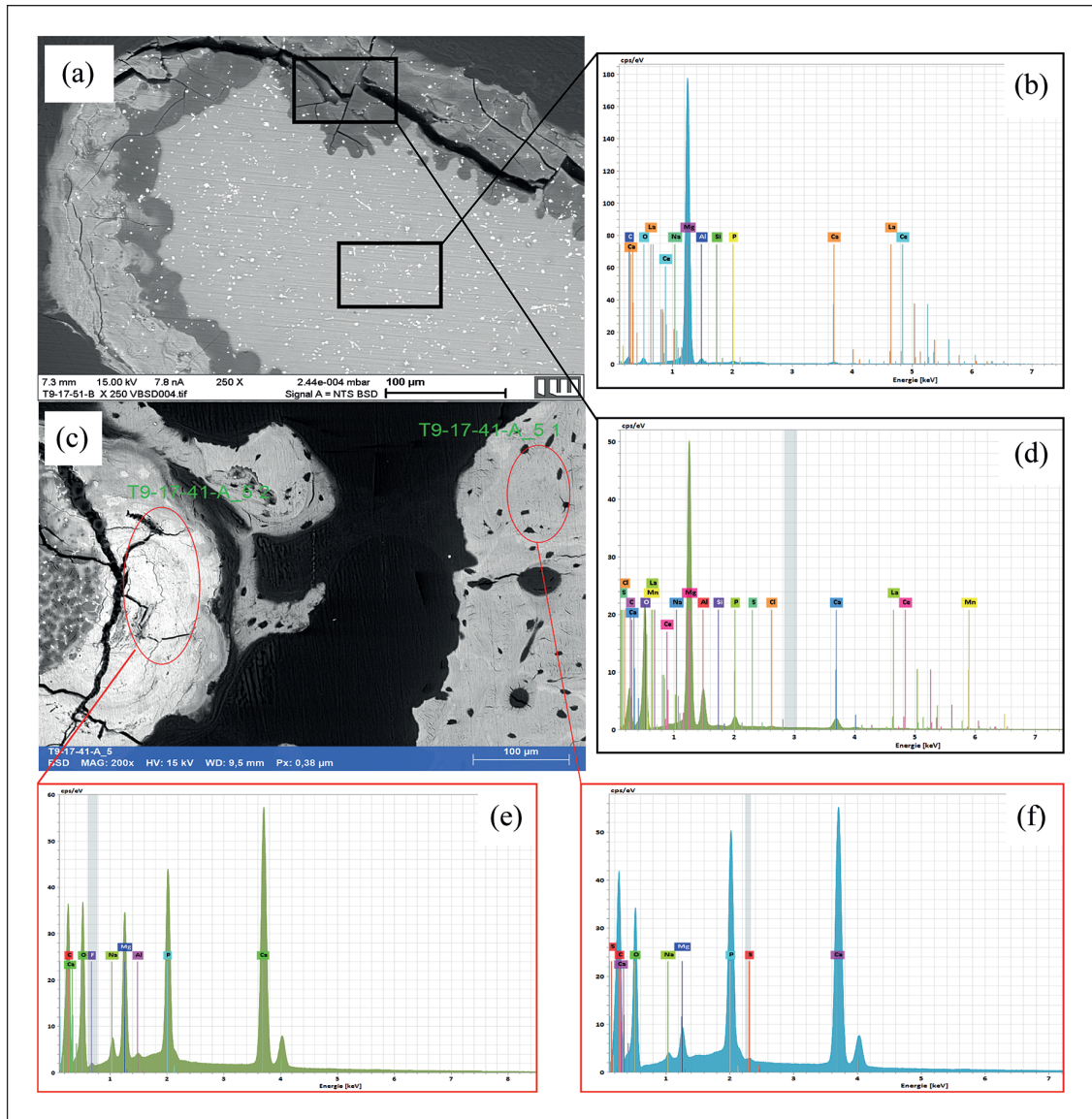
Figure 5. Exemplary SEM images of p500 after 24 weeks (a, b, and d) and SEM image of p400 after 6 weeks (c, e, and f) at the edge of the LAE442 scaffolds with associated EDX measurements. (a): The non-corroded, light gray base alloy differs significantly from the darker degradation layer. The distributed bright spots represent the rare earths as alloying elements. (b and d): EDX mappings in which the Mg content in the degradation layer is reduced and the Ca and P content in the degradation layer is increased. (c): SEM image of p400 with associated EDX measurements of (e) the Ca-P precipitates adjacent to the scaffolds and (f) bone tissue outside the scaffolds.

(Figure 8(a)–(d)). The gas vacuoles were delimited by fine borders of fibrocytes (Figure 8(b) and (c)). Blood vessels were frequently visible in the two outer regions (II and III) of both LAE442 pore sizes (Figure 8(c) and (d)). Blood vessels in the center (I) of p500 were found more frequently compared to p400 at all examination times, even if only small quantities could be detected. P500 showed significantly higher vascular ingrowth across the scaffold cross-section compared to p400 at week 6 ($p = 0.005$). Overall, p400 showed a higher amount of fibrocytes inside its scaffold structure than p500 with a significant

difference between both types at week 24 ($p < 0.001$). Strands of fibrocytes were distributed between individual struts in p400 in weeks 6 and 12 and were also found in the surrounding area (Figure 8(b)). However, a distinct capsule formation around the LAE442 scaffolds was never observed. In both LAE442 pore sizes, a moderate amount of macrophages and single foreign body giant cells (FBGC) were observed over time. Significantly more macrophages were found in p400 at week 6 compared to p500 ($p = 0.005$). At the interface between bone and the Mg alloy, both LAE442 pore sizes showed few FBGC with

incorporated material debris. These cell types were mainly arranged in clusters in the granulation tissue (Figure 8(c) and (d)). Concerning ß-TCP, myeloid cells, corresponding to physiological bone marrow, were found within the ceramic from week 6 onward, together with few fibrocytes and small blood vessels. Macrophages were seen sporadically. Figure 9 shows the occurrence of the different tissue and cell types for the individual scaffold groups. In both LAE442 pore sizes, granulation tissue dominated between the gas vacuoles, while bone marrow cells could be found to a much lesser extent than in ß-TCP. ß-TCP showed significantly fewer fibrocytes compared to p400 ($p < 0.001$, all evaluated times) and p500 ($p = 0.019$, week 6 and 12). Small amounts of granulocytes were visible inside and outside the ß-TCP scaffolds. This cell type was hardly present in p400 and p500, with a few exceptions in the peripheral environment.

Table 4. Corresponding EDX data showing elemental distribution (wt.%) at different locations. Locations investigated are shown in Figure 5 by using SEM imaging.

Element wt.%			
LAE442 p500 (week 24)		LAE442 p400 (week 6)	
Base material (non-corroded Mg alloy)	Degradation layer	Precipitation	Bone
Mg	91.58	72.68	13.71	3.22
Na	1.06	1.12	2.61	1.13
Al	2.89	12.91	0.34	–
Ca	1.73	6.78	60.96	67.66
P	1.04	3.80	21.93	27.68
F	–	–	0.46	–
S	–	0.13	–	0.32
Cl	–	0.38	–	–
Si	0.16	0.26	–	–
Mn	–	0.44	–	–
La	0.25	0.16	–	–
Cer	1.29	1.33	–	–

Discussion

In previous in vivo studies, the Mg alloy LAE442 in non-porous form has already proven to be a biocompatible, slowly degrading bone graft substitute with the property of maintaining mechanical integrity.[2,3,5,11,17–20,22] To achieve an ideal balance between degradation and replacement of the implant material with new bone,[30,38,42] integrated pores in the bone substitute material between 100 and 500 µm are supposed to have a beneficial effect regarding new bone ingrowth.[29,37] As a structural and osteoconductive component in bone substitutes, pores play an important role for a successful interaction between bone and implant.[29,31,37,45] The observation of an improved implant integration in bone tissue was confirmed by Lalk et al.,[7] using MgF$_2$ coated sponges of the Mg alloy AX30 with an irregular pore distribution in vivo. However, the influence of different pores of defined sizes on the degradation behavior and osteogenesis of Mg-based bone substitutes in vivo has only been described by Cheng et al.[14] The promising Mg alloy LAE442, which has primarily been investigated as a solid implant without pores,[2,3,5,11,17–20] has been described as an open-pored structure in vivo in studies by Kleer et al.[46] and Augustin et al.[40] In the present study, LAE442 was examined and compared for the first time as a scaffold with two different pore size models (p400 and p500) and a uniform geometry using high-resolution ex vivo µCT80 analysis to draw conclusions on degradation behavior and osseointegration. In addition, biocompatibility and tissue ingrowth into the pores of the Mg alloy were assessed using histological samples and compared with commercially available ß-TCP implants with the same outer dimensions. However, it was not possible to manufacture the ß-TCP implants with the same geometry as the porous LAE442. ß-TCP differs from LAE442 in terms of more diverse and inhomogeneous distributed pores which limits the comparison of both material groups. Despite this fact, the ceramic was chosen as a control because of its well-known good biocompatibility.[32,35,38,45] Nevertheless, it is important to keep in mind that ceramics do not achieve
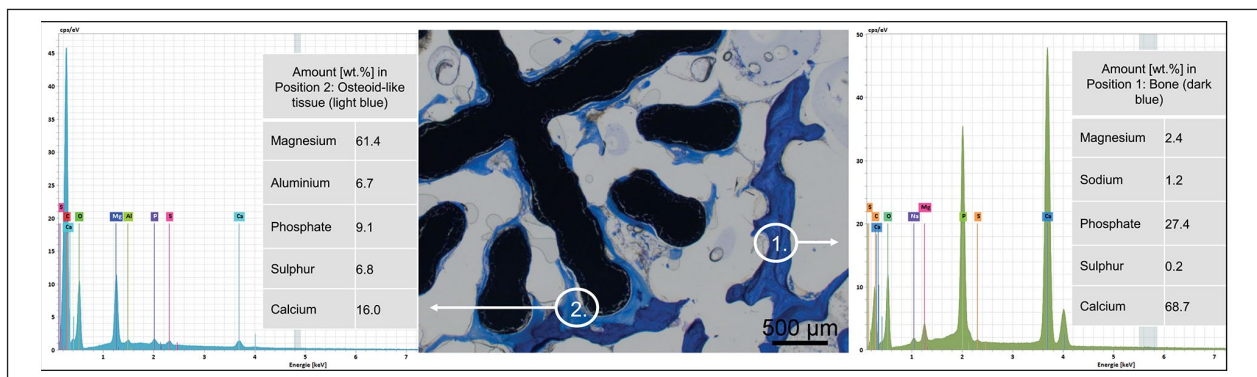
Figure 6. EDX analysis of the composition of bone tissue (circle 1) and osteoid-like tissue (OLT) (circle 2) in proximity to a p500 scaffold after 36 weeks.
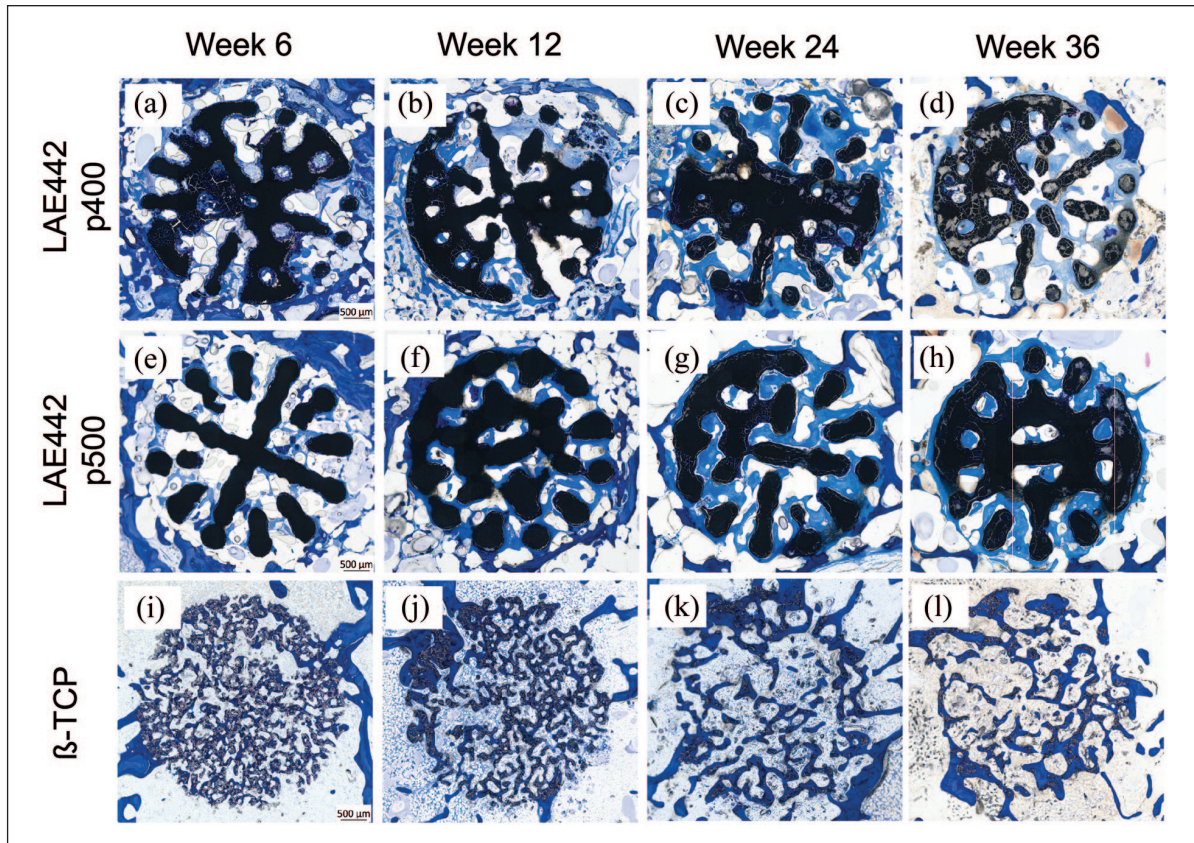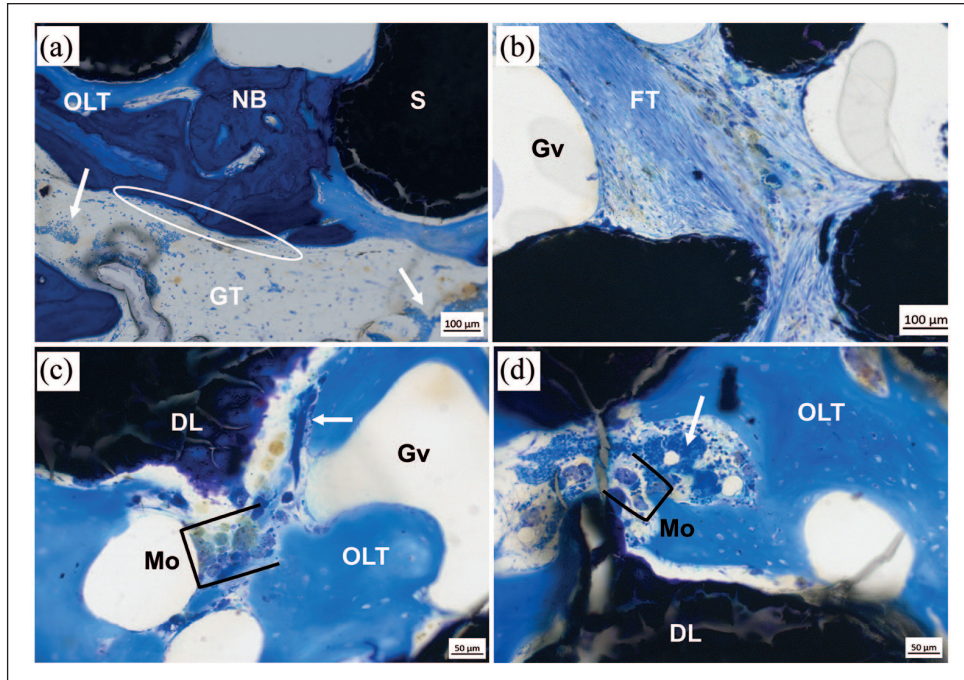
Figure 7. Toluidine blue staining of LAE442 p400, LAE442 p500 and ß-TCP cross-sections 6, 12, 24, and 36 weeks): (a–h) LAE442 scaffolds preserved the general shape, an increase in degradation is visible after 24 and 36 weeks; an increase in light blue osteoid-like tissue (OLT) is visible. Bone-scaffold contacts are visible in (a), (c), (e), (f), and (g); (i–l) residues of ß-TCP integrated by new bone.

a sufficient mechanical performance in weight-bearing bone defects without supportive fixation devices.[38]

Using high-resolution µCT80 after an implantation period of 36 weeks, semi-quantitative observations of a slow and steady degradation were consistent with quantitative volume losses of 7.5% for p500 and almost 10% for p400. Degradation rates concerning LAE442 have been described by others including Angrisani et al.,[19] who determined a slightly lower degradation of 4% in intramedullary LAE442 solid pins in rabbits after 36 weeks. Pitting corrosion, which was mainly visible at the strut edges of p400 over the entire study period, was also described by Witte et al.[39] who analyzed MgF_2 coated pins of LAE442 in femoral condyles of rabbits. Pitting corrosion occurs on the implant surface when the corrosion-decelerating MgF_2 layer is selectively degraded and the corrosion of the underlying exposed Mg alloy can progress locally to a greater extent.[47,48] According to literature,[49] the interaction of a dissolved coating and an increase in surface area represent local points of attack with chloride-containing body fluid, which can lead to an accelerated corrosion effect.[50–53] This effect could be transferred to p400, due to more frequently localized occurring pitting corrosion in the surface

topography. Further reasons for the more significant changes in shape and volume losses of p400 compared to p500, could be the rougher and somewhat larger surface area of p400 due to production.[54] A larger and more uneven surface displays a larger contact area of the implant material to the host tissue, which can result in a more rapid degradation.[29,55] A similar situation was described by Von der Höh et al.,[56] who investigated Mg implants with different surface structures in rabbit femura. They concluded that implants with a more uneven surface texture show a faster loss of structure and integrate to a lesser extent into cancelous bone than Mg implants with a smoother surface.

Since the corrosion process of Mg in physiological body fluid produces hydrogen gas,[50,57] a controllable amount of gas is considered as a key issue to be further improved for the surgical use of Mg as a resorbable bone substitute material.[22,49,50,58] During the course of the present study, gas in the p400 group diminished later in time compared to p500 and may have led to delayed drill hole closure for p400. This assumption corresponds to the in vivo study by Kraus et al.,[16] which investigated implanted Mg pins in the radius of rats for over 24 weeks. The

Figure 8. Toluidine blue staining of LAE442 scaffolds (12 and 24 weeks): (a) new bone in direct contact to the p500 surface, (b) arrangement of fibrous tissue within p400, (c) group of macrophages, osteoid-like tissue and gas vacuoles in close proximity to the degradation layer of the scaffold within p500, and (d) osteoid-like tissue and blood vessels within p500. Cracks within the alloy become apparent at the edges of the scaffold struts.
DL: degradation layer; FT: fibrous tissue; GT: granulation tissue; Gv: gas vacuoles; Mo: macrophage groups; NB: new bone; OLT: osteoid-like tissue; S: LAE442 scaffold; White arrows: blood vessels; white ellipse: osteoblasts.

implantation site was only closed completely when the gas decreased distinctly. Gas formation was also seen during degradation of LAE442 scaffolds in other in vivo studies but did not have a negative effect on clinical tolerability.[40,46] This was also conformed in studies on solid LAE442 implants in various animal models.[2,11,19,20,39]

Lu and Leng[59] observed an indication of good biocompatibility of a bone substitute material when new bone tissue forms in close vicinity to the implant. In the present study, this could be confirmed by various trabecular bone-scaffold contacts partially growing further into the pores. When comparing the pore sizes, a significantly higher number of bone-scaffold contacts were observed for p500 than for p400. According to Brånemark[60] and Mavrogenis et al.,[24] a higher number of bone-scaffold contacts indicates better integration. Trabeculae that have grown on and into p400 and p500 were finely formed. Observations of thin trabeculae being in the periphery of porous LAE442 implants matches with results in former in vivo studies on intramedullary LAE442 pins.[3,11,19] Ca-P precipitates, visible by SEM on the degradation layer and subsequently examined in the EDX, seem to be involved in creating the contact formation between bone and scaffold, as also observed by Witte et al.[2] and Thomann et al.[3] The precipitates, mainly enriched with Ca and P, are considered as a possible mineralization process origin for new bone formation according to Lu and Leng.[59] In the present study,

both LAE442 pore sizes were found to have more new bone tissue in the outer pore areas than in the central areas, with additional small bone fragments in the central part (CP) of the p500 scaffold. The presence of more bone in outer areas compared to more central areas was also described in AX30 Mg sponges after 24 weeks by Lalk et al.[7] The authors observed externally ingrown trabeculae and island-like bony structures more often in 400 μm pores than in smaller ones with 100 μm. A similar situation was also found in the work by Liu et al.[13] on pure Mg scaffolds after 3 months, in which new bone grew into the scaffolds starting from the outside, and after advanced Mg degradation, also proceeded into the interior of the scaffolds. Furthermore, this kind of bone ingrowth behavior was also observed in ceramics with different pore sizes[35,61,62] and macro-porous scaffolds made of silk fibroins.[63,64] In the present study, ß-TCP showed a larger number of partly ingrown bone-scaffold contacts in comparison to both LAE442 pore sizes. After 6 weeks, trabeculae already grew into central areas and led to significantly higher bone volume in the quantitative analyses than p400 and p500. Summarized over the entire study period, the bone bonding character of p400 and p500 was rather moderate and could have been more distinct, when compared to ß-TCP.

For the semi-quantitative histological evaluation, central histological cross-sections were chosen according to literature.[7,64] The material loss due to the cutting and
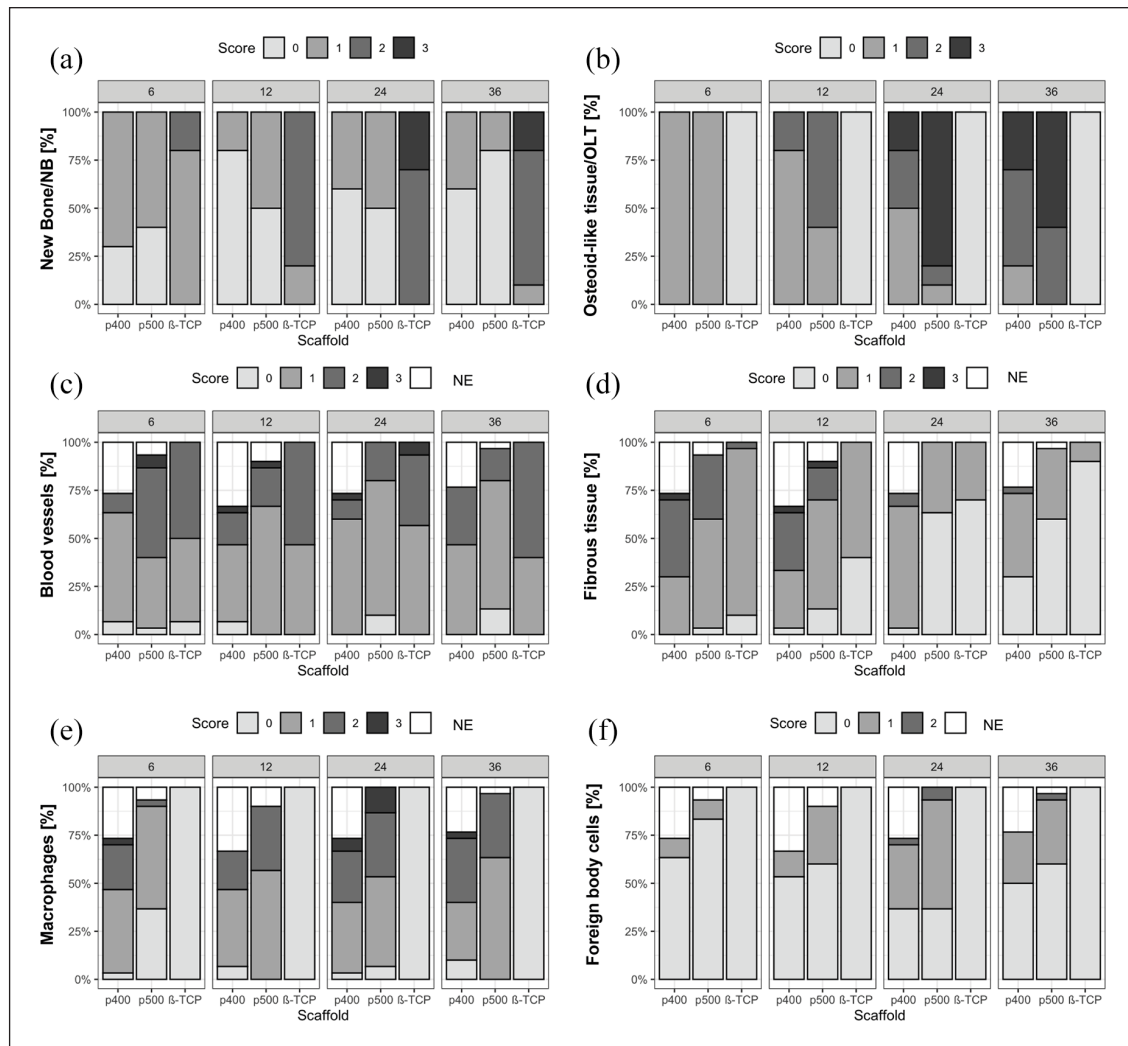
Figure 9. Results of the histological semi-quantitative scoring: (a) new bone/NB, (b) osteoid-like tissue/OLT, (c) blood vessels, (d) fibrous tissue, (e) macrophages, and (f) foreign body cells. The diagrams reflect the percentage distribution of the scores assigned to the mentioned parameters, which were examined on cross-sections of p400, p500, and ß-TCP in the respective weeks. Score values ranging from score 0 (none or 0%) to score 3 (many/or >25%) are described in detail in Table 2. NE (not evaluable): Cross-sections that had to be excluded due to technical preparation issues.

grinding technique, in combination with the geometric scaffold architecture, was a challenge. It was not possible to obtain standardized cross-sectional areas in the exact same level with the same fractions of pore or strut layers present in order to undergo precise and convincing histo-morphometry.[65,66] To avoid this bias in the data,[65] a semi-quantitative analysis was considered as a rather valuable tool for obtaining general trends of scaffold-tissue interaction.[63] This limitation is largely compensated by the possibility of a complete, nondestructive 3D calculation of quantitative trabecular bone parameters and scaffold components across the entire region of interest from the μCT scans.[17,67]

In the histological sections a cracked, granular degradation layer was seen on the outer struts of the LAE442 scaffolds suggesting material debris. This layer, which was formed during Mg corrosion, was also described by Angrisani et al.[19] and Dziuba et al.[12] P400 histologically showed a slightly greater tendency concerning surface cracking, significant differences to p500 were absent at most of the investigation time points. These histological observations indicate, analogous to the quantitative volume analyses and morphological changes in μCT80/SEM, a faster and more irregular degradation of p400 compared to p500. Additionally, it should be mentioned that cracks formed in the implants could also be artifacts that were created during histological processing (cutting, grinding).[4,68]

Beginning in week 6, newly formed bone (NB) surrounded by osteoid-like tissue (OLT) was observed in the pores of both LAE442. However, compared to ß-TCP, significantly less NB was found in p400 and p500, with no significant difference between both LAE442 pore sizes.

The observed difference in the amount of newly ingrown bone between ß-TCP and the LAE442 pore sizes may be attributed to the faster bioresorption of ß-TCP[32,38] and the significantly slower degradation behavior of the Mg alloy.[2–4,18–20] Cao and Kuboyama[32] also observed that the bone ingrowth determined over time was significantly lower when using slowly degrading bone substitutes than using faster degrading ones. Compared to the good bone-ceramic interaction, NB, which had grown into both LAE442 pore sizes, often had no direct contact with the inner surface of the LAE442 scaffolds. OLT visible in the present study between scaffold material and NB in histologically stained sections was also observed by Lalk et al.[7] within sponges of Mg alloy AX30. They assumed that OLT was barely mineralized as it did not appear to be of a bone like density in the μCT80. This assumption could be supported in the present study by additional SEM/EDX analyses, as OLT showed significantly reduced Ca- and P-contents compared to mature bone. In contrast to physiological osteoid seams of about 20 μm,[69] the OLT determined in the present study and by Lalk et al.[7] was more than ten times wider. Lined-up osteoblasts at the rim of the OLT in the present study as well as embedded osteocytes within the OLT and the degree of mineralization could suggest a preliminary stage of mature bone.[7] Parfitt et al.[70] also referred to osteoid as tissue on the way to mineralization and as a kind of pre-bone. In the literature, various causes for increased osteoid production are described. One reason could be the MgF_2 treated surface of the LAE442 alloy.[71–73] Another could be the influence of the high Mg content in the LAE442 alloy itself.[74,75] Stimulating effects of fluoride on osteoblasts and subsequent increased osteoid formation with delayed calcification were observed in mice.[71] However, this had no further influence on the microhardness of the trabecular structures.[71] Studies in rabbits also described a fluoride associated proliferation of the osteoid.[72,73] Mg ions released during the degradation process are also thought to promote the further differentiation of bone precursor cells, and thus could be the cause of increased osteoid deposition.[74,75] Systemic homeostasis of Mg is being maintained through intestinal absorption and the effective excretory pathway via the kidneys in healthy organisms.[76,77] Around 99% of magnesium is stored in bones, muscles, and soft tissues.[78] Based on some in vitro and in vivo studies in recent years, it is argued that the local excess of Mg ions released by corrosion may have a restraining effect on potential new bone tissue and cell viability.[15,79,80] The local pH increase at the interface may also lead to a reduced osteogenic differentiation of stem cells, which may further cause cellular non-adhesion or even non-mineralization.[15] In the present LAE442 study a close bone/OLT contact with the Mg alloy was continuously present within both pore sizes of LAE442. This indicates a good osteoconductive effect according to Fischerauer et al.[51] Similarly, to the present results, a

distinct contact was also observed by Witte et al.[81] and Lalk et al.[7] Both authors described enlarged osteoid seams[81] or extended amounts of osteoid tissue[7] during in vivo degradation. In the present study, more in-depth investigations of the OLT were carried out (local EDX measurements), but the lack of mineralization due to possible local factors as described above could not be clarified, the question of whether mature bone develops from OLT still needs to be addressed, although the selected observation period was considerably longer than the chosen study period of Lalk et al.[7] Serum analyses and histological organ examinations were performed in the past and showed no systemic or local signs of toxic or inflammatory tendencies.[12,19,20,39,82–86] The present study can confirm these findings from clinical examinations together with the fact that only few inflammatory cells were present in the histologic evaluation.

Cell penetration and the ingrowth of oxygen and nutrient-providing vessels is a prerequisite for successful bone regeneration within bone substitute materials of various origins.[28,29] The amount of blood vessels in the scaffolds interior determined in the granulation tissue showed no significant differences between LAE442 and ß-TCP. Pore size comparisons of just under 100 up to 400 μm demonstrated that the larger macroporous structures tended to show better vascularization.[7,31,63] Klenke et al.[31] described a correlation of increasing pore size with the more pronounced vascularization and osseointegration effect on biphasic Ca-P ceramic particles in cranial defects of mice. A trend toward better blood vessel supply within 400 μm large pores compared to the 100 μm pore model was also described for the Mg alloy AX30 by Lalk et al.[7] In the current study, the reported effect of increased vascularization in the larger pore size could only be confirmed in week 6 for p500, because afterward the score values of p400 and p500 converged. The difference in the two pore sizes was possibly not large enough to obtain more pronounced differences in this study.

The increased incidence of fibrocytes in p400 compared to p500, together with the significantly lower vascularization of p400 at week 6, confirms the assumption that reduced oxygenation promotes the formation of mesenchymal fibrous tissue.[87] Other in vivo studies investigating Mg scaffolds with pore sizes between 100 and 400 μm[7,14] also reported an increased fibrous tissue content or capsule formation around the smaller pore size. Despite moderate amounts of fibrous tissue, macrophages, and locally and sporadically occurring FBGCs, a thick capsule formation as described in Nuss and von Rechenberg[38] was not seen in both LAE442 pore sizes in the present study. The absence of fibrous capsules generally enables the formation of a good bone-implant contact. Bone bonding can form to varying degrees in bioresorbable materials such as Mg alloys, due to the continuous progress of in vivo corrosion and the erosive scaffold surfaces.[38] Therefore, it seems likely that bone-scaffold contacts do not have such a

permanent character as for example in non-degradable metals or within bioabsorbable ceramics. Additionally, the absence of fibrous capsules in the present study over 36 weeks indicates good long-term biocompatibility of the slowly degrading LAE442 scaffolds, as other studies on solid LAE442 pins previously reported.[11,19,20] Since macrophages and FBGCs also occurred as a cellular response in vivo in other Mg alloys[8–10] and biomaterials of non-metallic origin,[63,64,88] their presence is not automatically considered to be a pathological or abnormal reaction between implant material and host tissue.[38] There is a controversial debate about the general character of FBGCs and macrophages. Nevertheless, they can be interpreted as physiological or cellular responses to slowly biodegradable bone substitutes, as long as their presence does not exceed a certain level.[38,89,90] According to Nuss and von Rechenberg[38] a persistent inflammation, marked by lymphocytes, plasma cells, and neutrophil granulocytes combined with a thick, fibrous capsule therefore suggests non-biocompatible properties. These prerequisites, especially in combination and to such an extent, were not given in the present study.

Angrisani et al.[19] also attributed the presence of macrophages and FBGs after 3.5 years of implantation of LAE442 solid implants in rabbits, to the still proceeding implant degradation in order to remove corrosion products and described the extent of the cellular reaction as absolutely acceptable. In general, the surrounding tissue shows a varying degree of foreign body reaction, depending on the degradation rate of the Mg alloy used.[19,38] In contrast, Dziuba et al.[12] observed that degradation products can lead to inflammatory defense reactions in the host tissue when using much faster degrading implants like the Mg alloy ZEK100. Such a defense reaction, which is triggered by implant debris, did not occur during the entire duration of the study with the slowly degrading LAE442 scaffolds. Nevertheless, based on the literature and the current observations of the present study, this reaction seems to be typical for degradable biomaterials.[38,89,90]

Conclusion

The present study demonstrates that bone ingrowth generally occurred in both LAE442 pore size models. LAE442 p500 showed more successful osseointegration compared to p400, which was characterized by more bone-scaffold contacts and a greater tendency to show newly formed bone, even in central scaffold areas. The increased occurrence of OLT in direct contact with the LAE442 alloy makes p500 appear to be a more osteoconductive pore size model than p400. However, the osseointegration behavior of LAE442 was not equally as good compared to ß-TCP. The degradation of both LAE442 scaffolds continued steadily with low volume losses and tolerable gas formation due to degradation. Within the entire study period, a moderate number of macrophages and only a few FBGC were present within the histological specimens. Lower amounts of fibrocytes within LAE442 p500 compared to p400 suggest better biocompatibility together with more suitable osseointegrative properties for the larger pore size LAE442 p500. Crucial factors for the properties mentioned could be scaffolds with optimized surface coatings and pore sizes above 500 µm in combination with controlled gas release and continuous removal of corrosion products. Further studies on pore sizes, even larger than the mostly recommended range, may also provide further clarity. In this study, the LAE442 scaffolds have been exposed to low forces only. The suitability for repairing load-bearing defects cannot yet be finally clarified on the base of this study and therefore requires further studies on a weight-bearing experimental setting.

ORCID iD

Julia Augustin ![ORCID] https://orcid.org/0000-0002-2319-3912

References

1. Damien CJ and Parsons JR. Bone graft and bone graft substitutes: a review of current technology and applications. *J Appl Biomater* 1991; 2: 187–208.
2. Witte F, Kaese V, Haferkamp H, et al. In vivo corrosion of four magnesium alloys and the associated bone response. *Biomaterials* 2005; 26: 3557–3563.
3. Thomann M, Krause C, Bormann D, von der Höh N, Windhagen H and Meyer-Lindenberg A. Comparison of the resorbable magnesium alloys LAE442 und MgCa0.8 concerning their mechanical properties, their progress of degradation and the bone-implant-contact after 12 months implantation duration in a rabbit model. *Materwiss Werksttech* 2009; 40: 82–87.
4. Krause A, von der Höh N, Bormann D, et al. Degradation behaviour and mechanical properties of magnesium implants in rabbit tibiae. *J Mater Sci* 2010; 45: 624–632.
5. Meyer-Lindenberg A, Thomann M, Krause A, et al. Untersuchungen zum Einsatz einer Magnesiumbasislegierung als neues resorbierbares Implantatmaterial für die Osteosynthese. *Kleintierpraxis* 2010; 55: 349–363.
6. Lalk M, Reifenrath J, Rittershaus D, Bormann D and Meyer-Lindenberg A. Biocompatibility and degradation behaviour of degradable magnesium sponges coated with bioglass – method establishment within the framework of a pilot study. *Materwiss Werksttech* 2010; 41: 1025–1034.
7. Lalk M, Reifenrath J, Angrisani N, et al. Fluoride and calcium-phosphate coated sponges of the magnesium alloy AX30 as bone grafts: a comparative study in rabbits. *J Mater Sci Mater Med* 2013; 24: 417–436.
8. Reifenrath J, Krause A, Bormann D, von Rechenberg B, Windhagen H and Meyer-Lindenberg A. Profound differences in the in-vivo-degradation and biocompatibility of two very similar rare-earth containing Mg-alloys in a rabbit model. *Materwiss Werksttech* 2010; 41: 1054–1061.
9. Erdmann N, Bondarenko A, Hewicker-Trautwein M, et al. Evaluation of the soft tissue biocompatibility of MgCa0.8 and surgical steel 316L in vivo: a comparative study in rabbits. *Biomed Eng Online* 2010; 9: 63.
10. Huehnerschulte TA, Reifenrath J, von Rechenberg B, et al. In vivo assessment of the host reactions to the biodegradation of the two novel magnesium alloys ZEK100 and AX30 in an animal model. *Biomed Eng Online* 2012; 11(1): 4.
11. Hampp C, Angrisani N, Reifenrath J, Bormann D, Seitz JM and Meyer-Lindenberg A. Evaluation of the biocompatibility of two magnesium alloys as degradable implant materials in comparison to titanium as non-resorbable material in the rabbit. *Mater Sci Eng C Mater Biol Appl* 2013; 33: 317–326.
12. Dziuba D, Meyer-Lindenberg A, Seitz JM, Waizy H, Angrisani N and Reifenrath J. Long-term in vivo degradation behaviour and biocompatibility of the magnesium alloy ZEK100 for use as a biodegradable bone implant. *Acta Biomater* 2013; 9: 8548–8560.
13. Liu YJ, Yang ZY, Tan LL, Li H and Zhang YZ. An animal experimental study of porous magnesium scaffold degradation and osteogenesis. *Braz J Med Biol Res* 2014; 47: 715–720.
14. Cheng MQ, Wahafu T, Jiang GF, et al. A novel open-porous magnesium scaffold with controllable microstructures and properties for bone regeneration. *Sci Rep* 2016; 6: 24134.
15. Yu W, Zhao H, Ding Z, et al. In vitro and in vivo evaluation of MgF2 coated AZ31 magnesium alloy porous scaffolds for bone regeneration. *Colloids Surf B Biointerfaces* 2017; 149: 330–340.
16. Kraus T, Fischerauer SF, Hänzi AC, Uggowitzer PJ, Löffler JF and Weinberg AM. Magnesium alloys for temporary implants in osteosynthesis: in vivo studies of their degradation and interaction with bone. *Acta Biomater* 2012; 8: 1230–1238.
17. Witte F, Fischer J, Nellesen J, et al. In vitro and in vivo corrosion measurements of magnesium alloys. *Biomaterials* 2006; 27: 1013–1018.
18. Angrisani N, Seitz J-M, Meyer-Lindenberg A, et al. Rare earth metals as alloying components in magnesium implants for orthopaedic applications. In: Waldemar AM (ed.) *New features on magnesium alloys*. Rijeka: IntechOpen, 2012, pp.82–96.
19. Angrisani N, Reifenrath J, Zimmermann F, et al. Biocompatibility and degradation of LAE442-based magnesium alloys after implantation of up to 3.5years in a rabbit model. *Acta Biomater* 2016; 44: 355–365.
20. Rössig C, Angrisani N, Helmecke P, et al. In vivo evaluation of a magnesium-based degradable intramedullary nailing system in a sheep model. *Acta Biomater* 2015; 25: 369–383.
21. Marco F, Milena F, Gianluca G and Vittoria O. Peri-implant osteogenesis in health and osteoporosis. *Micron* 2005; 36: 630–644.
22. Staiger MP, Pietak AM, Huadmai J and Dias G. Magnesium and its alloys as orthopedic biomaterials: a review. *Biomaterials* 2006; 27: 1728–1734.
23. Sennerby L, Thomsen P and Ericson LE. A morphometric and biomechanic comparison of titanium implants inserted in rabbit cortical and cancellous bone. *Int J Oral Maxillofac Implants* 1992; 7: 62–71.
24. Mavrogenis AF, Dimitriou R, Parvizi J and Babis GC. Biology of implant osseointegration. *J Musculoskelet Neuronal Interact* 2009; 9: 61–71.
25. Rosenqvist R, Bylander B, Knutson K, et al. Loosening of the porous coating of bicompartmental prostheses in patients with rheumatoid arthritis. *J Bone Joint Surg Am* 1986; 68: 538–542.
26. Mombelli A and Cionca N. Systemic diseases affecting osseointegration therapy. *Clin Oral Implants Res* 2006; 17 Suppl 2(l): 97–103.
27. Zhang H, Lewis CG, Aronow MS and Gronowicz GA. The effects of patient age on human osteoblasts' response to Ti-6Al-4V implants in vitro. *J Orthop Res* 2004; 22: 30–38.
28. Kuboki Y, Takita H, Kobayashi D, et al. BMP-induced osteogenesis on the surface of hydroxyapatite with geometrically feasible and nonfeasible structures: topology of osteogenesis. *J Biomed Mater Res* 1998; 39: 190–199.
29. Karageorgiou V and Kaplan D. Porosity of 3D biomaterial scaffolds and osteogenesis. *Biomaterials* 2005; 26: 5474–5491.
30. Phemister D. The fate of transplanted bone and regenerative power of its various constituents. *Surg Gyn Obst* 1914; 19: 303–314.

31. Klenke FM, Liu Y, Yuan H, Hunziker EB, Siebenrock KA and Hofstetter W. Impact of pore size on the vascularization and osseointegration of ceramic bone substitutes in vivo. *J Biomed Mater Res* 2008; 85: 777–786.

32. Cao H and Kuboyama N. A biodegradable porous composite scaffold of PGA/beta-TCP for bone tissue engineering. *Bone* 2010; 46: 386–395.

33. Tsuruga E, Takita H, Itoh H, Wakisaka Y and Kuboki Y. Pore size of porous hydroxyapatite as the cell-substratum controls BMP-induced osteogenesis. *J Biochem* 1997; 121: 317–324.

34. Götz HE, Müller M, Emmel A, Holzwarth U, Erben RG and Stangl R. Effect of surface finish on the osseointegration of laser-treated titanium alloy implants. *Biomaterials* 2004; 25: 4057–4064.

35. von Doernberg M-C, von Rechenberg B, Bohner M, et al. In vivo behavior of calcium phosphate scaffolds with four different pore sizes. *Biomaterials* 2006; 27: 5186–5198.

36. Willie BM, Yang X, Kelly NH, et al. Osseointegration into a novel titanium foam implant in the distal femur of a rabbit. *J Biomed Mater Res Part B Appl Biomater* 2010; 92: 479–488.

37. Hulbert SF, Young FA, Mathews RS, Klawitter JJ, Talbert CD and Stelling FH. Potential of ceramic materials as permanently implantable skeletal prostheses. *J Biomed Mater Res* 1970; 4: 433–456.

38. Nuss KMR and von Rechenberg B. Biocompatibility issues with modern implants in bone – a review for clinical orthopedics. *Open Orthop J* 2008; 2: 66–78.

39. Witte F, Fischer J, Nellesen J, et al. In vivo corrosion and corrosion protection of magnesium alloy LAE442. *Acta Biomater* 2010; 6: 1792–1799.

40. Augustin J, Feichtner F, Waselau A-C, et al. Comparison of two pore sizes of LAE442 scaffolds and their effect on degradation and osseointegration behavior in the rabbit model. *J Biomed Mater Res Part B Appl Biomater* 2020; 108: 2776–2788.

41. Seitz J-M, Collier K, Wulf E, et al. The effect of different sterilization methods on the mechanical strength of magnesium based implant materials. *Adv Eng Mater* 2011; 13: 1146–1151.

42. Julmi S, Krüger A-K, Waselau A-C, et al. Processing and coating of open-pored absorbable magnesium-based bone implants. *Mater Sci Eng C Mater Biol Appl* 2019; 98: 1073–1086.

43. Thomann M, Krause C, Angrisani N, et al. Influence of a magnesium-fluoride coating of magnesium-based implants (MgCa0.8) on degradation in a rabbit model. *J Biomed Mater Res A* 2010; 93: 1609–1619.

44. Donath K and Breuner G. A method for the study of undecalcified bones and teeth with attached soft tissues. *J Oral Pathol Med* 1982; 11: 318–326.

45. Kasten P, Beyen I, Niemeyer P, Luginbühl R, Bohner M and Richter W. Porosity and pore size of β-tricalcium phosphate scaffold can influence protein production and osteogenic differentiation of human mesenchymal stem cells: an in vitro and in vivo study. *Acta Biomater* 2008; 4: 1904–1915.

46. Kleer N, Julmi S, Gartzke AK, et al. Comparison of degradation behaviour and osseointegration of the two magnesium scaffolds, LAE442 and La2, in vivo. *Materialia* 2019; 8: 100436.

47. Makar GL and Kruger J. Corrosion of magnesium. *Int Mater Rev* 1993; 38(3): 138–153.

48. Staesche M. Über die chemische Erzeugung einer dickeren Magnesiumfluorid-Schutzschicht auf Magnesium-Legierungen. *Arch Metallkunde* 1948; 3: 99–102.

49. Song GL and Atrens A. Corrosion mechanisms of magnesium alloys. *Adv Eng Mater* 1999; 1: 11–33.

50. Zeng R, Dietzel W, Witte F, Hort N and Blawert C. Progress and challenge for magnesium alloys as biomaterials. *Adv Eng Mater* 2008; 10: B3–B14.

51. Fischerauer SF, Kraus T, Wu X, et al. In vivo degradation performance of micro-arc-oxidized magnesium implants: a micro-CT study in rats. *Acta Biomater* 2013; 9: 5411–5420.

52. Wang YQ, Zheng MY and Wu K. Microarc oxidation coating formed on SiCw/AZ91 magnesium matrix composite and its corrosion resistance. *Mater Lett* 2005; 59: 1727–1731.

53. Gu Y, Chen CF, Bandopadhyay S, Ning C, Zhang Y and Guo Y. Corrosion mechanism and model of pulsed DC microarc oxidation treated AZ31 alloy in simulated body fluid. *Appl Surf Sci* 2012; 258(16): 6116–6126.

54. Julmi S, Klose C, Krüger A-K, et al. Development of sponge structure and casting conditions for absorbable magnesium bone implants. In: TMS T (ed.) *TMS 2017; 146th annual meeting & exhibition supplemental proceedings*. Cham: Springer, 2017, pp.307–317.

55. Wolters L, Angrisani N, Seitz J, Helmecke P, Weizbauer A and Reifenrath J. Applicability of degradable magnesium LAE442 alloy plate-screw-systems in a rabbit model. *Biomed Tech* 2013; 58(1). DOI: 10.1515/bmt-2013-4059.

56. Von der Höh N, Bormann D, Lucas A, et al. Influence of different surface machining treatments of magnesium-based resorbable implants on the degradation behavior in rabbits. *Adv Eng Mater* 2009; 11: B47–B54.

57. Witte F, Hort N, Vogt C, et al. Degradable biomaterials based on magnesium corrosion. *Curr Opin Solid State Mater Sci* 2008; 12: 63–72.

58. Yazdimamaghani M, Razavi M, Vashaee D, Moharamzadeh K, Boccaccini AR and Tayebi L. Porous magnesium-based scaffolds for tissue engineering. *Mater Sci Eng C Mater Biol Appl* 2017; 71: 1253–1266.

59. Lu X and Leng Y. Theoretical analysis of calcium phosphate precipitation in simulated body fluid. *Biomaterials* 2005; 26(10): 1097–1108.

60. Brånemark PI. Osseointegration and its experimental background. *J Prosthet Dent* 1983; 50(3): 399–410.

61. Theiss F, Apelt D, Brand B, et al. Biocompatibility and resorption of a brushite calcium phosphate cement. *Biomaterials* 2005; 26: 4383–4394.

62. Chu TM, Orton DG, Hollister SJ, Feinberg SE and Halloran JW. Mechanical and in vivo performance of hydroxyapatite implants with controlled architectures. *Biomaterials* 2002; 23: 1283–1293.

63. Hofmann S, Hilbe M, Fajardo RJ, et al. Remodeling of tissue-engineered bone structures in vivo. *Eur J Pharm Biopharm* 2013; 85(1): 119–129.

64. Uebersax L, Apfel T, Nuss KM, et al. Biocompatibility and osteoconduction of macroporous silk fibroin implants in cortical defects in sheep. *Eur J Pharm Biopharm* 2013; 85: 107–118.

65. Maglio M, Salamanna F, Brogini S, et al. Histological, histomorphometrical, and biomechanical studies of bone-implanted medical devices: Hard resin embedding. *Biomed Res Int* 2020; 2020: 1804630.

66. Rüegsegger P, Koller B and Müller R. A microtomographic system for the nondestructive evaluation of bone architecture. *Calcif Tissue Int* 1996; 58: 24–29.

67. Wachter NJ, Augat P, Krischak GD, Mentzel M, Kinzl L and Claes L. Prediction of cortical bone porosity in vitro by microcomputed tomography. *Calcif Tissue Int* 2001; 68: 38–42.

68. Kraus T, Fischerauer S, Treichler S, et al. The influence of biodegradable magnesium implants on the growth plate. *Acta Biomater* 2018; 66: 109–117.

69. Raina V. Normal osteoid tissue. *J Clin Pathol* 1972; 25: 229–232.

70. Parfitt AM, Drezner MK, Glorieux FH, et al. Bone histomorphometry: standardization of nomenclature, symbols, and units. Report of the ASBMR Histomorphometry Nomenclature Committee. *J Bone Miner Res* 1987; 2: 595–610.

71. Mousny M, Omelon S, Wise L, et al. Fluoride effects on bone formation and mineralization are influenced by genetics. *Bone* 2008; 43: 1067–1074.

72. Susheela AK and Jha M. Cellular and histochemical characteristics of osteoid formed in experimental fluoride poisoning. *Toxicol Lett* 1983; 16: 35–40.

73. McCormack AP, Anderson PA and Tencer AF. Effect of controlled local release of sodium fluoride on bone formation: filling a defect in the proximal femoral cortex. *J Orthop Res* 1993; 11: 548–555.

74. Zreiqat H, Howlett CR, Zannettino A, et al. Mechanisms of magnesium-stimulated adhesion of osteoblastic cells to commonly used orthopaedic implants. *J Biomed Mater Res* 2002; 62: 175–184.

75. Revell PA, Damien E, Zhang XS, Evans P and Howlett CR. The effect of magnesium ions on bone bonding to hydroxyapatite coating on titanium alloy implants. *Key Eng Mater* 2003; 254–256: 447–450.

76. Saris N-EL, Mervaala E, Karppanen H, Khawaja JA and Lewenstam A. Magnesium: an update on physiological, clinical and analytical aspects. *Clin Chim Acta* 2000; 294: 1–26.

77. Vormann J. Magnesium: nutrition and metabolism. *Mol Aspects Med* 2003; 24: 27–37.

78. Elin RJ. Assessment of magnesium status for diagnosis and therapy. *Magnes Res* 2010; 23: S194–S198.

79. Yoshizawa S, Brown A, Barchowsky A and Sfeir C. Magnesium ion stimulation of bone marrow stromal cells enhances osteogenic activity, simulating the effect of magnesium alloy degradation. *Acta Biomater* 2014; 10: 2834–2842.

80. Wong HM, Wu S, Chu PK, et al. Low-modulus Mg/PCL hybrid bone substitute for osteoporotic fracture fixation. *Biomaterials* 2013; 34: 7016–7032.

81. Witte F, Ulrich H, Palm C and Willbold E. Biodegradable magnesium scaffolds: part II: peri-implant bone remodeling. *J Biomed Mater Res A* 2007; 81: 757–765.

82. Zhang E, Xu L, Yu G, Pan F and Yang K. In vivo evaluation of biodegradable magnesium alloy bone implant in the first 6 months implantation. *J Biomed Mater Res* 2009; 90: 882–893.

83. Zhang S, Zhang X, Zhao C, et al. Research on an Mg–Zn alloy as a degradable biomaterial. *Acta Biomater* 2010; 6: 626–640.

84. Diekmann J, Bauer S, Weizbauer A, et al. Examination of a biodegradable magnesium screw for the reconstruction of the anterior cruciate ligament: a pilot in vivo study in rabbits. *Mater Sci Eng C Mater Biol Appl* 2016; 59: 1100–1109.

85. Xu L, Yu G, Zhang E, Pan F and Yang K. In vivo corrosion behavior of Mg-Mn-Zn alloy for bone implant application. *J Biomed Mater Res* 2007; 83: 703–711.

86. Li Z, Gu X, Lou S and Zheng Y. The development of binary Mg-Ca alloys for use as biodegradable materials within bone. *Biomaterials* 2008; 29: 1329–1344.

87. Muschler GF, Nakamoto C and Griffith LG. Engineering principles of clinical cell-based tissue engineering. *J Bone Joint Surg Am* 2004; 86: 1541–1558.

88. Bergsma EJ, Rozema FR, Bos RR and de Bruijn WC. Foreign body reactions to resorbable poly(l-lactide) bone plates and screws used for the fixation of unstable zygomatic fractures. *J Oral Maxillofac Surg* 1993; 51: 666–670.

89. Lassus J, Salo J, Jiranek WA, et al. Macrophage activation results in bone resorption. *Clin Orthop Relat Res* 1998; 1998: 7–15.

90. Anderson JM. Inflammation, wound healing, and the foreign-body response. In: Ratner B, Hoffmann A, Schoen FJ, et al. (eds) *Biomaterials science*. San Diego, CA: Elsevier, 2004, pp.296–303.

Appendix A: Guidelines for accommodation and care of animals

Council of Europe. European Convention for the Protection of Vertebrate Animals used for Experimental and other Scientific Purposes (ETS No. 123). Council of Europe. Strasbourg, 1986.